nature nanotechnology

LETTERS

PUBLISHED ONLINE: 15 APRIL 2012 | DOI: 10.1038/NNANO.2012.50

A robust scanning diamond sensor for nanoscale imaging with single nitrogen-vacancy centres

P. Maletinsky[1†], S. Hong[2†], M. S. Grinolds[1†], B. Hausmann[2], M. D. Lukin[1], R. L. Walsworth[1,3], M. Loncar[2] and A. Yacoby[1*]

The nitrogen-vacancy defect centre in diamond[1–4] has potential applications in nanoscale electric and magnetic-field sensing[2–6], single-photon microscopy[7,8], quantum information processing[9] and bioimaging[10]. These applications rely on the ability to position a single nitrogen-vacancy centre within a few nanometres of a sample, and then scan it across the sample surface, while preserving the centre's spin coherence and readout fidelity. However, existing scanning techniques, which use a single diamond nanocrystal grafted onto the tip of a scanning probe microscope[2,8,11,12], suffer from short spin coherence times due to poor crystal quality, and from inefficient far-field collection of the fluorescence from the nitrogen-vacancy centre. Here, we demonstrate a robust method for scanning a single nitrogen-vacancy centre within tens of nanometres from a sample surface that addresses both of these concerns. This is achieved by positioning a single nitrogen-vacancy centre at the end of a high-purity diamond nanopillar, which we use as the tip of an atomic force microscope. Our approach ensures long nitrogen-vacancy spin coherence times (~75 μs), enhanced nitrogen-vacancy collection efficiencies due to waveguiding, and mechanical robustness of the device (several weeks of scanning time). We are able to image magnetic domains with widths of 25 nm, and demonstrate a magnetic field sensitivity of 56 nT $Hz^{-1/2}$ at a frequency of 33 kHz, which is unprecedented for scanning nitrogen-vacancy centres.

Nitrogen-vacancy (NV)-based nanoscale sensing is possible because the NV centre forms a bright and stable single-photon source[13] for optical imaging and has a spin-triplet ground state that offers excellent magnetic[3] and electric[5] field sensing capabilities. The remarkable performance of the NV centre in such spin-based sensing schemes is the result of the long NV spin coherence time[14], combined with efficient optical spin preparation and readout[15]. These properties persist from cryogenic temperatures to ambient conditions, a feature that distinguishes the NV centre from other systems proposed as quantum sensors, such as single molecules[16] or quantum dots[1]. Reducing the distance between the NV centre and the sample of interest is crucial for improving spatial resolution. Past experiments aimed at implementing scanning NV microscopes were focused on grafting diamond nanocrystals onto scanning probe tips[2,8]. Although used successfully in the past, this approach suffers from the poor sensing performance of nanocrystal-based NV centres, for which the spin coherence times are typically orders of magnitude shorter than for NVs in bulk diamond[3]. Here, we present a novel approach that overcomes these drawbacks and thereby realizes the full potential of bulk NV-based sensing schemes in the scanning geometry relevant for nanoscale imaging. In particular, we have developed a monolithic 'scanning NV sensor' (Fig. 1a), which uses a diamond nanopillar as the scanning probe, with an individual NV centre artificially created within ~10 nm of the pillar tip through ion implantation[17]. Long NV spin coherence times are achieved as our devices are fabricated from high-purity, single-crystalline bulk diamond, which brings the additional advantage of high mechanical robustness. Furthermore, diamond nanopillars are efficient waveguides for the NV fluorescence band[18], which for a scanning NV device yields record-high NV signal collection efficiencies.

Figure 1b shows a representative scanning electron microscope (SEM) image of a single-crystalline diamond scanning probe containing a single NV centre within ~10 nm of its tip. To prepare such devices, a series of fabrication steps are performed sequentially, including low-energy ion implantation for NV creation, several successively aligned electron-beam lithography steps and reactive ion etching[19]. An essential element to this sequence is the fabrication of micrometre-thin, single-crystalline diamond slabs that form the basis of the scanning probe device shown in Fig. 1b. A detailed description of the fabrication procedure of these slabs and the resulting devices can be found in the Methods. Our scanning diamond nanopillars have typical diameters of ~200 nm and lengths of 1 μm and are fabricated on few-micrometre-sized diamond platforms that are individually attached to atomic force microscope (AFM) tips for scanning (see Fig. 1b and Methods for details of the attaching process). Our fabrication procedure (Fig. 1c) allows for highly parallel processing, as shown in the array of diamond devices depicted in the SEM image in Fig. 1d. Close to 30% of the diamond nanopillars in our samples contain single, negatively charged NV centres. Other devices contain more than one NV, or one NV in a charge-neutral state, which is unsuitable for magnetometry. From these 30%, we select the NV centres that exhibit the highest photon count rates and longest spin coherence times and mount these single-NV nanopillars onto AFM tips to yield the finalized scanning probe shown in the SEM picture in Fig. 1b. We note that these scanning devices were fabricated from a [001]-oriented diamond crystal, resulting in NV orientation and magnetic-field sensing along an axis tilted by 54.7° from the nanopillar direction.

To use the scanning NV sensor and characterize its basic spin and optical properties, we used a combined confocal and atomic force microscope as sketched in Fig. 1a. The set-up was equipped with piezo positioners for the sample and an AFM head to allow for independent scanning with respect to the optical axis. Optical addressing and readout of the NV centre was performed through a long-working-distance microscope objective (numerical aperture,

[1]Department of Physics, Harvard University, Cambridge, Massachusetts 02138, USA, [2]School of Engineering and Applied Science, Harvard University, Cambridge Massachusetts 02138, USA, [3]Harvard–Smithsonian Center for Astrophysics, Cambridge, Massachusetts 02138, USA; †These authors contributed equally to this work. *e-mail: yacoby@physics.harvard.edu

© 2012 Macmillan Publishers Limited. All rights reserved.

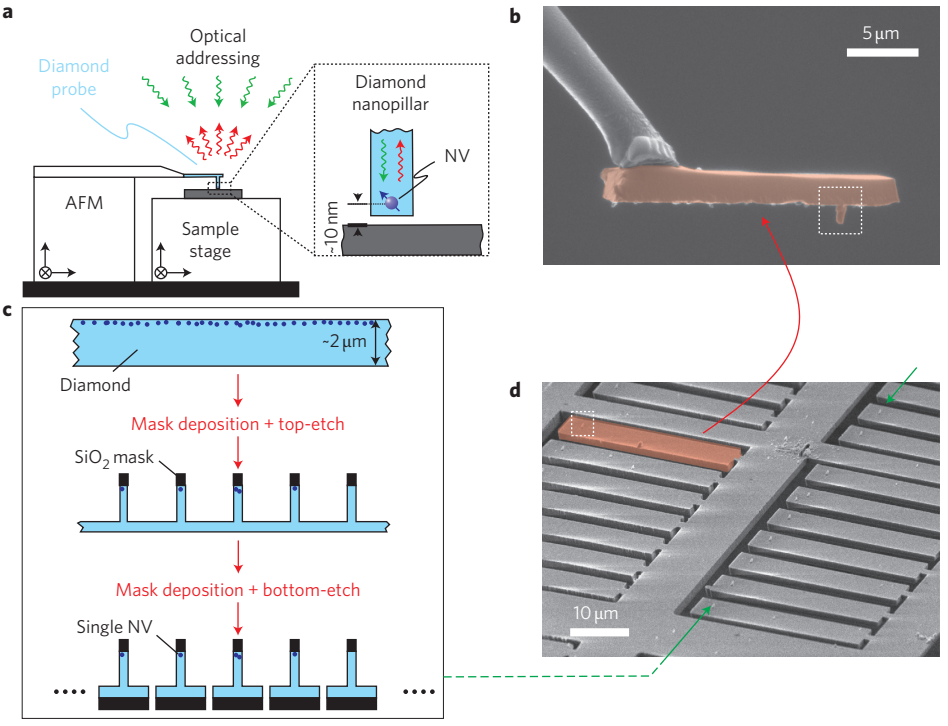


Figure 1 | Experimental set-up and probe fabrication for the scanning NV sensor. a, Schematic of the set-up, consisting of a combined optical and atomic force microscope (AFM). We use a 532 nm laser (green arrows) to address the scanning NV centre through its red fluorescence (red arrows). The scanning NV centre resides in a diamond nanopillar (inset) and its proximity to the sample is maintained by means of AFM feedback. **b**, SEM image of a single-crystalline diamond nanopillar probe (false colour coded in red) with a single NV centre in its tip (see Fig. 2). **c**, Brief depiction of the fabrication process for scanning single-crystalline diamond NV sensors. Electron-beam lithography is used to define nanopillars and platforms from the top and bottom sides of a few-micrometre thin diamond membrane. Patterns are then transferred to the diamond by reactive ion etching. **d**, SEM image of a finalized array of diamond platforms with nanopillars. In all panels, dotted rectangles highlight diamond nanopillars.

NA = 0.7). Microwave radiation for coherent NV spin manipulation was applied using a gold bonding wire attached in proximity to the NV centre (see Methods).

Figure 2a shows a confocal scan under green laser illumination (excitation wavelength, 532 nm) of a typical single scanning NV device. The bright photon emission emerging from the nanopillar (white circle) originates from a single NV centre, as indicated by the pronounced dip in the photon-autocorrelation measurement (Fig. 2b) and the characteristic signature of optically detected NV electron-spin resonance (ESR)[15] (Fig. 2c), all obtained on the same device. Importantly, we confirm that photon waveguiding through the nanopillar[18] persists despite the close proximity of the NV to the tip of our fabricated nanopillar devices. For example, the data in Fig. 2c were obtained at 100 μW excitation power and demonstrate single NV counts approaching 2.2×10^5 counts per second (c.p.s.)—an approximately fivefold increase in detected fluorescence intensity compared to an NV observed under similar conditions in an unpatterned diamond sample. We thus significantly increase the fluorescence signal strength from the scanning NV and at the same time minimize exposure of the samples to green excitation light, which is especially relevant for possible biological or low-temperature applications of the scanning NV sensor.

Using well-established techniques for coherent NV-spin manipulation[20], we characterized the spin coherence time T_2 of the same NV centre studied so far. Spin-coherence sets the NV sensitivity to magnetic fields and limits the number of coherent operations that can be performed on an NV spin; it is therefore an essential figure of merit for applications in magnetic-field imaging[4] and quantum information processing[9]. Using a Hahn-echo pulse sequence, we measured the characteristic single NV coherence decay[21] shown in Fig. 2d; from the decay envelope we deduce a spin coherence time of $T_2 = 74.8$ μs. We note that this T_2 time is consistent[4] with the density of implanted nitrogen ions (3×10^{11} cm^{-2}) and conclude that our device fabrication procedure fully preserves NV spin coherence. Combining measurements of the T_2 time with the fluorescence count rate and NV spin readout contrast as obtained in Fig. 2, we obtain a maximal 'a.c.' magnetic field sensitivity[4] of 56 nT Hz$^{-1/2}$ at a frequency of 33 kHz and (based on data in Fig. 2c) a 'd.c.' sensitivity of 6.0 μT Hz$^{-1/2}$. We note that both a.c. and d.c. magnetic field sensitivities could be further improved by using spin-decoupling sequences[22] and optimized parameters for spin readout[23], respectively.

To characterize the resolving power of the scanning NV sensor, we imaged a nanoscale magnetic memory medium consisting of bit tracks of alternating (out-of-plane) magnetization with various bit sizes. Figure 3 illustrates our method and results. The scanning NV sensor operated in a mode that imaged contours of constant magnetic field strength (B_{NV}) along the NV axis through the continuous monitoring of red NV fluorescence, in the presence of an ESR driving field of fixed frequency ω_{MW} and typical magnitude $B_{MW} \approx 2$ G (as determined from NV Rabi oscillations, not shown). We detuned ω_{MW} by δ_{MW} from the bare NV spin transition frequency ω_{NV}, but local magnetic fields due to the sample changed this detuning during image acquisition. In particular, when local fields brought the spin transition of the NV into resonance with ω_{MW}, we observed a drop in NV fluorescence rate, which in the image yielded a contour of constant of $B_{NV} = \delta_{MW}/\gamma_{NV}$, with $\gamma_{NV} = 2.8$ MHz G^{-1} being the NV gyromagnetic ratio. We simultaneously acquired two such images by applying radiofrequency sidebands to ω_{NV} with $\delta_{MW} = \pm 10$ MHz (dark and bright arrows in Fig. 3c). Normalization of the pixel values in the two data sets

© 2012 Macmillan Publishers Limited. All rights reserved.

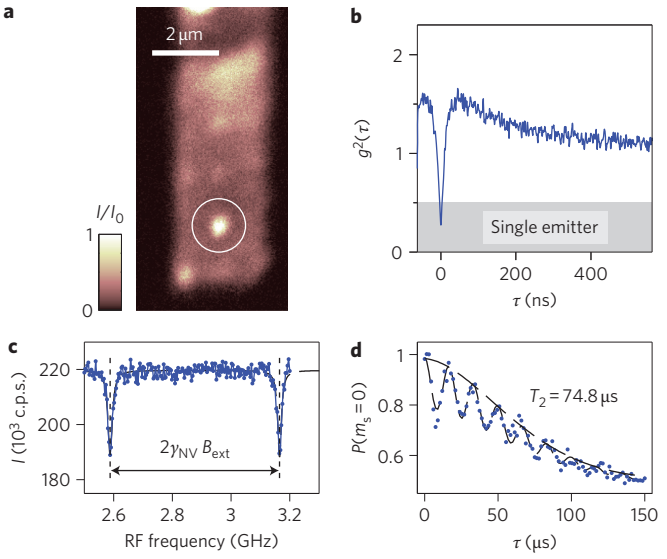


Figure 2 | A single NV centre in a scanning diamond nanopillar. a, Confocal image of red fluorescence from a single-crystalline diamond probe (see side view SEM image in Fig. 1b). Fluorescence counts are normalized to $I_0 = 1.5 \times 10^5$ c.p.s. The encircled bright feature stems from fluorescence of a single NV centre in the nanopillar. **b**, Photon autocorrelation measurement ($g^2(\tau)$) for NV fluorescence in the scanning nanopillar device. Data with $g^2 < 0.5$ (grey-shaded region) demonstrate the presence of a single photon emitter in the nanopillar. **c**, Optically detected ESR identifies the single emitter in the nanopillar as an NV centre. The two possible NV spin transitions[15] are split by the NV electron Zeeman splitting $2\gamma_{NV}B_{NV}$, where $\gamma_{NV} = 2.8$ MHz G^{-1} is the NV gyromagnetic ratio and B_{NV} is the magnetic field along the NV axis (here, $B_{NV} \approx 103$ G). **d**, Spin-echo measurement for the NV centre in the diamond nanopillar device. The envelope fitted to the characteristic NV spin-echo decay (see Methods) yields the NV spin coherence time of $T_2 = 74.8$ μs. Data in panels **b**–**d** were all taken on the same device. Green excitation power: 100 μW in **b**–**d**, and 400 μW in **a**.

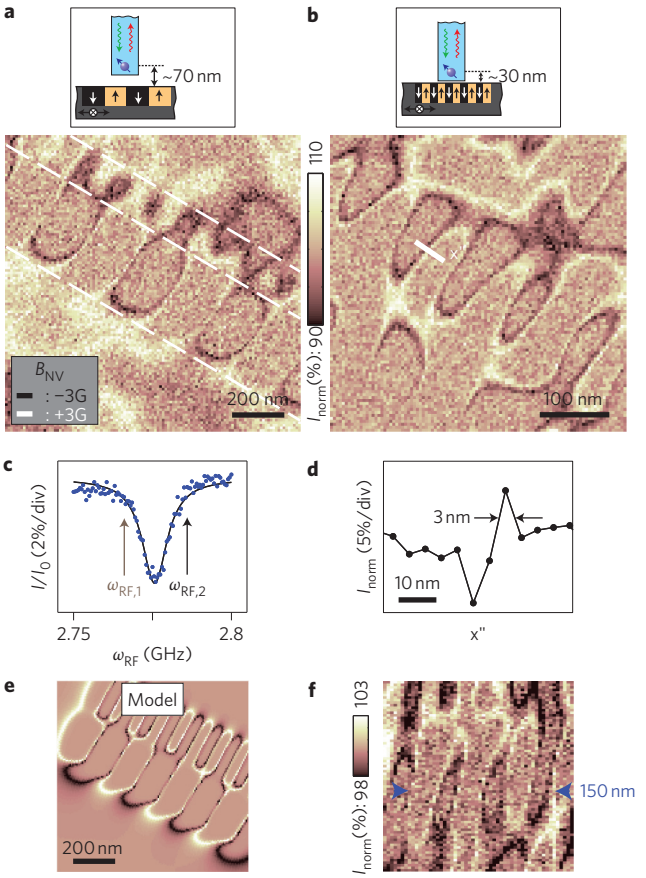


Figure 3 | Nanoscale magnetic-field imaging with the scanning NV sensor. **a**, NV magnetic field image of bit tracks on a magnetic memory, highlighted by dashed white lines. We plotted normalized data, $I_{norm} = I_{RF,1}/I_{RF,2}$ (see text and **c**), to reveal magnetic field lines corresponding to a sample magnetic field along the NV axis of $B_{NV} = \pm 3$ G (see inset). Additionally, a bias magnetic field of $B_{NV} \approx 52$ G was applied to determine the sign of the measured magnetic fields. **b**, Magnetic image obtained as in **a**, but with the NV–sample distance decreased by an estimated 50 nm. Bringing the NV closer to the sample increases the magnetic field magnitude at the NV sensor, and improves the imaging spatial resolution, allowing us to image magnetic bits, ~38 nm in width. Approximate NV–sample distances are noted in the schematics illustrating the experimental configuration, with the sensing NV centre fixed on the optical axis and the magnetic sample scanned below the pillar. Total image acquisition times were 11.2 min (50 ms per pixel) for **a** and 12.5 min (75 ms per pixel) for data in **b**, with laser powers of 130 μW. The colour bar applies to **a** and **b. c**, Optically detected ESR of the sensing NV centre. For magnetic-field imaging, we modulate an applied microwave field between two frequencies ($\omega_{RF,1} = 2.766$ GHz and $\omega_{RF,2} = 2.786$ GHz) and collect NV fluorescence counts ($I_{RF,1}$ and $I_{RF,2}$, respectively) in synchrony with the RF modulation. **d**, Line-cut along the white line indicated in **b** (averaged across six adjacent pixels) indicating the ability of the sensor to spatially distinguish magnetic field lines separated by ~3 nm (limited by the local magnetic field gradient). **e**, Calculated NV response for the experimental situation in **a**, assuming a simplified magnetic sample (Supplementary Section S1). **f**, Magnetic image as in **a** and **b** for a different experimental realization. Here, due to a further decrease in the NV–sample distance, the smallest observed domains have average sizes of 25 nm as determined for the six domains found in the 150 nm interval marked by the blue arrows. The reduced imaging contrast in **f** results from the close proximity of the NV to the sample (see text).

then directly provided a map of magnetic field contours with positive and negative values of B_{NV} (here, with $B_{NV} = \pm 3$ G) and at the same time helped to reject low-frequency noise[24]. Figure 3a shows a resulting scanning NV magnetometry image of two stripes of magnetic bits (indicated by the white dashed lines) with bit spacings of 170 nm and 65 nm. The shape of the observed domains is well reproduced by calculating the response of the NV magnetometer to an idealized sample with rectangular magnetic domains of dimensions corresponding to the written tracks (Fig. 3e and Supplementary Section S1).

The spatial resolution of an NV magnetometer is affected by the distance from the NV centre to the sample. Approaching the NV sensor more closely to the magnetic sample therefore revealed magnetic bits with average sizes of ~38 nm, as shown in Fig. 3b. We note that, in this image, due to the large field gradients generated at the boundaries between domains, we could observe transitions between magnetic field lines on length scales of ~3 nm (full-width at half-maximum of the line-cut in Fig. 3d). An even further decrease of NV–sample distance allowed us to image yet smaller domains, ~25 nm in width (Fig. 3f), but with a reduced imaging contrast caused by strong magnetic fields transverse to the NV axis, which occur in close vicinity to the surface of the sample[25] (Supplementary Section S2). One of the disadvantages of using a hard drive to characterize our tip is that the local magnetic fields are very large and exceed the typical dynamic range of our technique. However, such experiments provide valuable information regarding NV–sample distance, and consequently the spatial resolution achieved in imaging. In particular, we estimate the distance between the scanning NV and the sample to be comparable to 25 nm, based on the smallest magnetic domain sizes we observed.

© 2012 Macmillan Publishers Limited. All rights reserved.

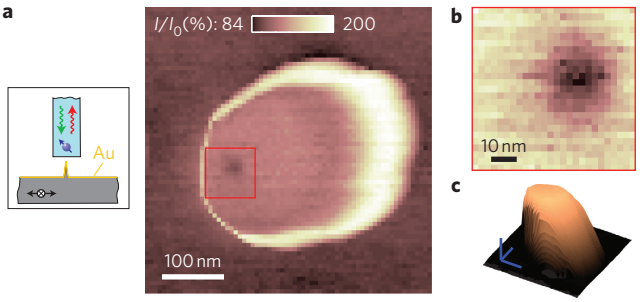


Figure 4 | Nanoscale fluorescence quenching imaging of the scanning NV sensor. a, Scanning the diamond pillar over a sharp metallic tip leads to a bright, circular feature due to the sample topography (see Supplementary Information). Positioning the metallic tip exactly at the location of the NV centre (red square), however, yields a sharp dip in NV fluorescence. The illustration shows the experimental configuration used in this experiment. **b**, Zoomed-in image of the red square region in **a**. The observed fluorescence quenching dip has a spatial resolution of ~20 nm. **c**, AFM topography image obtained simultaneously with the data in **b**. Blue scale bars represent 100 nm displacement in all directions. Image acquisition times were 30 min (320 ms per pixel) and 2.7 min (250 ms per pixel) in **a** and **b**, respectively, at a laser power of 35 μW.

To independently verify the proximity of the NV to the diamond surface, we conducted a measurement in which we scanned a sharp metallic tip (<20 nm in diameter, see schematic in Fig. 4a and Supplementary Section S4) over the NV-containing pillar to image the location of the NV. The imaging contrast consisted of the detected NV fluorescence in the far-field changing when the NV was located in close proximity to the metallic tip[26]. Owing to the strong dependence of NV fluorescence rate on the distance between the NV and the metallic sample[26] (here, due to partial fluorescence quenching and local modifications of excitation light intensity), we could use this technique to precisely locate the position of the NV centre within the diamond nanopillar. The resulting data (Fig. 4a) showed signatures of the topography of the scanning diamond nanopillar (bright ring in the NV fluorescence signal, see Supplementary Section S5 for details). More importantly, however, while the front-end of the diamond probe scanned over the sharp metallic tip, we observed a dip in NV fluorescence (red square in Fig. 4a and zoomed image in Fig. 4b) when the metallic tip was positioned at the location of the NV centre. This feature is not accompanied by any topographic features and is thus attributed to partial quenching of the NV fluorescence due to the sharp metallic tip (see Fig. 4c and Supplementary Section S5). The Gaussian width (double standard deviation) of 25.8 nm of this fluorescence quenching spot was probably still limited by the size of the metallic tip and therefore marks an upper bound to our ability to localize the NV centre within the pillar. Importantly, such data allow us to find the position of the single NV centre with respect to the topography of our device (Fig. 4c), which will greatly facilitate precise alignment of our sensing NV centre with respect to (magnetic) targets in future sensing and imaging applications.

The biggest remaining uncertainty to the distance between the scanning NV centre and the sample is vertical straggle in the NV implantation process, which is still poorly understood[24]. Naturally occurring stable NV centres have been observed as close as 3 nm from diamond surfaces[27], so future advances in the controlled creation of NV centres[28] should allow us to further improve the NV–sample distance and therefore the spatial resolution in scanning NV imaging by about one order of magnitude. Additionally, the coherence properties of artificially created NV centres close to the diamond surface could be further improved by appropriate annealing techniques[29] or dynamical decoupling[22], which would both significantly improve the magnetic sensing capabilities of the scanning NVs. We note that for magnetic field imaging, our current ability to resolve individual magnetic domains already equals the typical performance of alternative methods[30,31], with the added advantages of being non-invasive and quantitative.

The magnetic field sensitivity we demonstrated here with the scanning NV sensor compares well to the performance realized previously with single NV centres in ultrapure, bulk diamond samples[3]. Additionally, the mechanical robustness and durability of our diamond probes (up to several weeks of scanning with the same tip) illustrate the advantage of our method over alternative approaches to scanning NV magnetometry[2,8]. Compared with other physical systems used for nanoscale magnetic imaging, NV centres in monolithic diamond scanning probes stand out due to the excellent photostability of the NVs, the possibility of room-temperature operation and the chemical inertness of diamond, which allow for magnetometry operation even under harsh environmental conditions.

To conclude, we note that the scope of applications of our scanning NV probe extends far beyond magnetic imaging. For example, our devices are ideally suited to use as optical sensors[7,16] and form an interesting platform to coherently couple the scanning NV spin to other spin systems such as phosphorus in silicon[32], other NV centres, or carbon-based spin qubits[33]. Quantum information could thereby be transferred between a stationary qubit and our scanning NV centre, and from there to single photons[34] or other qubit systems such as long-lived nuclear spin qubits in the diamond matrix.

Note added in proof. During the preparation of the manuscript, we learned of related work, performed independently by Rondin and colleagues[12].

Methods

Diamond tip fabrication. Devices were fabricated from a sample of high-purity, single-crystalline diamond (Element Six, electronic grade; thickness 50 μm). We implanted the sample with atomic nitrogen at an energy of 6 keV and density of 3×10^{11} cm^{-2} (leading to a nominal mean NV depth of ~10 nm). Subsequent annealing at 800 °C for 2 h yielded a shallow layer of NV centres with a density of ~25 NVs/μm^2 and a depth of ~10 nm. We then etched the sample from the non-implanted side to a thickness of ~3 μm using reactive ion etching (RIE, Unaxis shuttleline). We used a cyclic etching recipe consisting of a 10 min $ArCl_2$ (ref. 35) etch, followed by 30 min of O_2 (ref. 19) etching and a cooling step of 15 min. This sequence was essential to maintain the integrity of the diamond surface during the few-hour etching time. On the resulting thin diamond membrane, we fabricated an array of diamond nanopillars on the top side by using electron-beam lithography and RIE as described previously[19]. Next, we performed a second lithography step on the back-side of the diamond slab, which defined platforms to hold the diamond nanopillars. A final RIE process transferred the resist pattern to the sample, and fully cut through the diamond membrane to yield the structure shown in Fig. 1d.

To mount a pre-selected diamond platform on an AFM tip, we used a focused ion beam (FIB) system (Zeiss NVision 40) equipped with a nanomanipulator (Omniprobe AutoProbe 300) and ion-assisted metal deposition. We used tungsten deposition to fuse a diamond platform to a quartz AFM tip and then used FIB cutting to release the diamond platform from the bulk. With a properly aligned FIB, this process does not contaminate the scanning diamond nanopillar, and yields an NV/AFM probe as shown in Fig. 1b.

Combined confocal and atomic force microscope. We used a home-built microscope combining optical (confocal) imaging and AFM. The optical microscope was based on a long-working-distance microscope objective (Mitutoyo ULWD HR NIR ×100, 0.7 NA). The AFM was tuning-fork-based, controlled using commercial electronics (Attocube ASC500) and mounted using a home-built AFM head. Both the sample and the AFM head were fixed on three-axis coarse and fine positioning units (Attocube ANPxyz101 and ANSxyz100, respectively) to allow positioning of the diamond tip with respect to the fixed optical axis and subsequent scanning of the sample with respect to the diamond probe.

Optical excitation of the NV centre was performed using a diode-pumped solid-state laser (LaserGlow LRS-0532-PFM-00100-01) at a wavelength of 532 nm. Pulsed excitation for coherent NV spin manipulation used a double-pass acousto-optical modulator (AOM) set-up (Isomet, AOM 1250C-848). ESR was driven with a microwave generator (Rhode Schwartz, SMB100A) and amplifier (MiniCircuits, ZHL-42W). The ESR field was delivered to the NV centre through a gold bonding wire (diameter, 25 μm) mounted as a short-cut termination to a semirigid coaxial cable.

© 2012 Macmillan Publishers Limited. All rights reserved.

The wire was brought into close proximity (~50 μm) of the scanning NV to minimize the required RF power. Both the microwave source and the AOM were timed using a computer-controlled trigger card (Spincore, PulseBlasterESR-PRO-400).

Fit to spin-echo data. To obtain the NV T_2 time from the spin-echo measurement presented in Fig. 2d, we fitted the data to a sum of Gaussian peaks, modulated by a decay envelope $\propto \exp[-(\tau/T_2)^n]$; that is, we used the fit function[36]:

$$\exp[-(\tau/T_2)^n] \sum_j \exp[-((\tau - j\tau_{rev})/T_{dec})^2]$$

Taking T_2, n, τ_{rev} and T_{dec} as free fitting parameters, we found $T_2 = 74.8 \pm 4.3$ μs, $n = 1.7 \pm 0.2$, $\tau_{rev} = 16.7 \pm 0.1$ μs and $T_{dec} = 7.6 \pm 0.2$ μs for the data shown in Fig. 2d (errors indicate 95% confidence intervals for the nonlinear least-squares parameter estimates).

Received 8 February 2012; accepted 13 March 2012; published online 15 April 2012

References

1. Chernobrod, B. M. & Berman, G. P. Spin microscope based on optically detected magnetic resonance. *J. Appl. Phys.* **97,** 014903 (2005).
2. Balasubramanian, G. *et al.* Nanoscale imaging magnetometry with diamond spins under ambient conditions. *Nature* **455,** 648–651 (2008).
3. Maze, J. R. *et al.* Nanoscale magnetic sensing with an individual electronic spin in diamond. *Nature* **455,** 644–647 (2008).
4. Taylor, J. *et al.* High-sensitivity diamond magnetometer with nanoscale resolution. *Nature Phys.* **4,** 810–816 (2008).
5. Dolde, F. *et al.* Electric-field sensing using single diamond spins. *Nature Phys.* **7,** 459–463 (2011).
6. Degen, C. L. Scanning magnetic field microscope with a diamond single-spin sensor. *Appl. Phys. Lett.* **92,** 243111 (2008).
7. Sekatskii, S. & Letokhov, V. Nanometer-resolution scanning optical microscope with resonance excitation of the fluorescence of the samples from a single-atom excited center. *JETP Lett.* **63,** 319–323 (1996).
8. Cuche, A. *et al.* Near-field optical microscopy with a nanodiamond-based single-photon tip. *Opt. Express* **17,** 19969–19980 (2009).
9. Neumann, P. *et al.* Quantum register based on coupled electron spins in a room-temperature solid. *Nature Phys.* **6,** 249–253 (2010).
10. McGuinness, L. P. *et al.* Quantum measurement and orientation tracking of fluorescent nanodiamonds inside living cells. *Nature Nanotech.* **6,** 358–363 (2011).
11. Kuhn, S., Hettich, C., Schmitt, C., Poizat, J. & Sandoghdar, V. Diamond colour centres as a nanoscopic light source for scanning near-field optical microscopy. *J. Microsc.* **202,** 2–6 (2001).
12. Rondin, L. *et al.* Nanoscale magnetic field mapping with a single spin scanning probe magnetometer. *Appl. Phys. Lett.* (in the press).
13. Kurtsiefer, C., Mayer, S., Zarda, P. & Weinfurter, H. Stable solid-state source of single photons. *Phys. Rev. Lett.* **85,** 290–293 (2000).
14. Balasubramanian, G. *et al.* Ultralong spin coherence time in isotopically engineered diamond. *Nature Mater.* **8,** 383–387 (2009).
15. Gruber, A. *et al.* Scanning confocal optical microscopy and magnetic resonance on single defect centers. *Science* **276,** 2012–2014 (1997).
16. Michaelis, J., Hettich, C., Mlynek, J. & Sandoghdar, V. Optical microscopy using a single-molecule light source. *Nature* **405,** 325–328 (2000).
17. Kalish, R. *et al.* Nitrogen doping of diamond by ion implantation. *Diamond Relat. Mater.* **6,** 516–520 (1997).
18. Babinec, T. M. *et al.* A diamond nanowire single-photon source. *Nature Nanotech.* **5,** 195–199 (2010).
19. Hausmann, B. J. *et al.* Fabrication of diamond nanowires for quantum information processing applications. *Diamond Relat. Mater.* **19,** 621–629 (2010).
20. Jelezko, F., Gaebel, T., Popa, I., Gruber, A. & Wrachtrup, J. Observation of coherent oscillations in a single electron spin. *Phys. Rev. Lett.* **92,** 076401 (2004).
21. Van Oort, E. & Glasbeek, M. Optically detected low field electron spin echo envelope modulations of fluorescent N-V centers in diamond. *Chem. Phys.* **143,** 131–140 (1990).
22. De Lange, G., Ristè, D., Dobrovitski, V. V. & Hanson, R. Single-spin magnetometry with multipulse sensing sequences. *Phys. Rev. Lett.* **106,** 080802 (2011).
23. Dreau, A. *et al.* Avoiding power broadening in optically detected magnetic resonance of single NV defects for enhanced dc magnetic field sensitivity. *Phys. Rev. B* **84,** 195204 (2011).
24. Grinolds, M. S. *et al.* Quantum control of proximal spins using nanoscale magnetic resonance imaging. *Nature Phys.* **7,** 687–692 (2011).
25. Lai, N., Zheng, D., Jelezko, F., Treussart, F. & Roch, J-F. Influence of a static magnetic field on the photoluminescence of an ensemble of nitrogen-vacancy color centers in a diamond single-crystal. *Appl. Phys. Lett.* **95,** 133101 (2009).
26. Buchler, B. C., Kalkbrenner, T., Hettich, C. & Sandoghdar, V. Measuring the quantum efficiency of the optical emission of single radiating dipoles using a scanning mirror. *Phys. Rev. Lett.* **95,** 063003 (2005).
27. Bradac, C. *et al.* Observation and control of blinking nitrogen-vacancy centres in discrete nanodiamonds. *Nature Nanotech.* **5,** 345–349 (2010).
28. Pezzagna, S. *et al.* Nanoscale engineering and optical addressing of single spins in diamond. *Small* **6,** 2117–2121 (2010).
29. Naydenov, B. *et al.* Increasing the coherence time of single electron spins in diamond by high temperature annealing. *Appl. Phys. Lett.* **97,** 242511 (2010).
30. Wolny, F. *et al.* Iron filled carbon nanotubes as novel monopole-like sensors for quantitative magnetic force microscopy. *Nanotechnology* **21,** 435501 (2010).
31. Kohashi, T., Konoto, M. & Koike, K. High-resolution spin-polarized scanning electron microscopy (spin SEM). *J. Electron Microsc.* **59,** 43–52 (2010).
32. Kane, B. E. A silicon-based nuclear spin quantum computer. *Nature* **393,** 133–137 (1998).
33. Recher, P. & Trauzettel, B. Quantum dots and spin qubits in graphene. *Nanotechnology* **21,** 302001 (2010).
34. Togan, E. *et al.* Quantum entanglement between an optical photon and a solid-state spin qubit. *Nature* **466,** 730–734 (2010).
35. Lee, C., Gu, E., Dawson, M., Friel, I. & Scarsbrook, G. Etching and micro-optics fabrication in diamond using chlorine-based inductively-coupled plasma. *Diamond Relat. Mater.* **17,** 1292–1296 (2008).
36. Childress, L. *et al.* Coherent dynamics of coupled electron and nuclear spin qubits in diamond. *Science* **314,** 281–285 (2006).

Acknowledgements

The authors thank B.D. Terris and N. Supper from Hitachi GST for providing the magnetic recording samples. P.M. acknowledges support from the Swiss National Science Foundation and S.H. thanks the Kwanjeong Scholarship Foundation for funding. M.S.G. is supported by fellowships from the Department of Defense (NDSEG programme) and the National Science Foundation (NSF). This work was supported by NIST and DARPA QuEST and QuASAR programmes and in part was performed at the Center for Nanoscale Systems (CNS), a member of the National Nanotechnology Infrastructure Network (NNIN), which is supported by the NSF (under award no. ECS–0335765). CNS is part of Harvard University.

Author contributions

All authors contributed to all aspects of this work.

Additional information

The authors declare no competing financial interests. Supplementary information accompanies this paper at www.nature.com/naturenanotechnology. Reprints and permission information is available online at http://www.nature.com/reprints. Correspondence and requests for materials should be addressed to A.Y.

© 2012 Macmillan Publishers Limited. All rights reserved.